Energy Storage Materials xxx (xxxx) xxx

Contents lists available at ScienceDirect

Energy Storage Materials

journal homepage: www.elsevier.com/locate/ensm

Local structure adaptability through multi cations for oxygen redox accommodation in Li-Rich layered oxides

Enyue Zhao [a,b,1], Minghao Zhang [c,1], Xuelong Wang [a], Enyuan Hu [d], Jue Liu [e,**], Xiqian Yu [a,b,*], Marco Olguin [c], Thomas A. Wynn [c], Ying Shirley Meng [c,***], Katharine Page [e], Fangwei Wang [a,b,f], Hong Li [a,b], Xiao-Qing Yang [d], Xuejie Huang [a], Liquan Chen [a]

[a] Beijing National Laboratory for Condensed Matter Physics, Institute of Physics, Chinese Academy of Sciences, Beijing, 100190, China
[b] Center of Materials Science and Optoelectronics Engineering, College of Materials Science and Opto-Electronic Technology, University of Chinese Academy of Sciences, Beijing, 100049, China
[c] Department of NanoEngineering, University of California San Diego, La Jolla, CA, 92093, USA
[d] Chemistry Division, Brookhaven National Laboratory, Upton, NY, 11973, USA
[e] Neutron Scattering Division, Oak Ridge National Laboratory, Oak Ridge, TN, 37831, USA
[f] Songshan Lake Materials Laboratory, Dongguan, Guangdong, 523808, China

ARTICLE INFO

Keywords:
Lithium-ion battery
Lithium-rich cathode
Lattice oxygen redox
Pair distribution function
Local structure

ABSTRACT

Stable lattice oxygen redox (l-OR) is the key enabler for achieving attainable high energy density in Li-rich layered oxide cathode materials for Li-ion batteries. However, the unique local structure response to oxygen redox in these materials, resulting in energy inefficiency and hysteresis, still remains elusive, preventing their potential applications. By combining the state-of-the-art neutron pair distribution function with crystal orbital overlap analysis, we directly observe the distinct local structure adaption originated from the potential O–O chemical bonds. The structure adaptability is optimized based on the nature of multi transition metals in our model compound $Li_{1.2}Ni_{0.13}Mn_{0.54}Co_{0.13}O_2$, which accommodates the oxygen redox and at the same time preserves the global layered structure. These findings not only advance the understanding of l-OR, but also provide new perspectives in the rational design of high-energy-density cathode materials with reversible and stable l-OR.

1. Introduction

Rechargeable lithium-ion batteries have promoted the development of (micro)electronics and are being considered as the technology of choice for large-scale energy storage fields, such as electric vehicles, smart grid. Intercalation-based layered transition metal (TM) oxides (e.g., $LiCoO_2$, $LiNi_xMn_yCo_{1-x-y}O_2$) is a typical cathode material whose electrochemical reactivity mainly based on the (de)intercalation of Li^+ ions (from)into the crystal lattice [1–5]. Simultaneously, a redox reaction in terms of the electron transfer occurs on TM ions to maintain the charge neutrality (i.e., charge compensation). The attainable specific capacity is thus limited by either the number of Li^+ ions existed in the cathode or the number of electrons that can be transferred from TM ions, and is closely correlated with the stability (or reversibility) of the layered structure.

The ascension of the Li-rich layered oxide (LRLO) cathode materials breaks this capacity limitation [6–8]. In this class of materials, other than the cationic (TM ions) redox, the extra charge compensation can be further provided by the lattice oxygen redox (l-OR) to achieve the ultrahigh capacity [9–17]. Unfortunately, the irreversible l-OR (e.g., O_2 release) usually cause inferior electrochemical behaviors (e.g., voltage fade and voltage hysteresis), which retards the practical application of LRLO materials [18,19]. Accordingly, researches have been conducted to understand and promote the l-OR reversibility. The results from both experiment and theory calculation have suggested that the covalency of TM-O has a strong impact on the reversibility of l-OR [10,11,20]. It was also indicated that there is a closely association between the l-OR stability and structure transformation reversibility [21]. In the meantime, peroxo-like O–O dimer [11] and isolated oxygen electron holes [9] were

* Corresponding author. Beijing National Laboratory for Condensed Matter Physics, Institute of Physics, Chinese Academy of Sciences, Beijing, 100190, China.
** Corresponding author.
*** Corresponding author.
E-mail addresses: liuj1@ornl.gov (J. Liu), xyu@iphy.ac.cn (X. Yu), shirleymeng@ucsd.edu (Y.S. Meng).
[1] E. Zhao and M. Zhang contributed equally to this work.

https://doi.org/10.1016/j.ensm.2019.07.032
Received 11 June 2019; Received in revised form 20 July 2019; Accepted 23 July 2019
Available online xxxx

proposed, respectively, to successfully stabilize the l-OR in the corresponding models. Additionally, strategies including surface modification, heteroatomic doping, etc. have been shown effective in advancing the stable l-OR [19,22–25]. However, to date, how to rational design/tailor LRLO materials to accommodate the l-OR and thus achieve its stable operation remains ambiguous.

To approach this issue, it is crucial to clarify the electronic and crystal structure response of LRLO materials to the l-OR. Localized structure evolution is challenging to be experimentally proved and quantified. Because it demands advanced characterization tools with both short-range sensitivity and global statistics. To detect both the local and average structure throughout the l-OR process, neutron pair distribution function (nPDF) analysis, capable of emphasizing the oxygen atomic scattering, was employed in this work. Li- and Mn-rich $Li_{1.2}Ni_{0.13}Mn_{0.54}Co_{0.13}O_2$ (LMR-NMC) was selected as the model compound considering the practical-application potential of 3d-TM-based LRLO materials. A local structure distortion (shrink of the O–O pair distance) accompanied with the l-OR was for the first time directly observed using nPDF in 3d-TM-based LRLO materials. It was found that this localized distorted oxygen lattice accommodates the l-OR preserving the global layered structure, which, in turn, promotes the reversibility and stability of the l-OR. Furthermore, crystal orbital overlap populations (COOPs) calculation was introduced as bonding descriptor for explaining local structure adaption. It was also found that the adaptability of oxygen lattice is highly dependent on the TM species (i.e., covalency of the TM-O bond). Based on these understandings, it was proposed that multi TM ions can be combined to achieve both the stable structure and reversible l-OR in LRLO materials.

2. Experimental section

2.1. Sample preparation

$Li_{1.2}Mn_{0.54}Ni_{0.13}Co_{0.13}O_2$ compound was prepared by a conventional solid-state reaction using stoichiometric lithium carbonate (5% excess of lithium) and the metal hydroxide with Mn: Ni: Co of 0.54: 0.13: 0.13 in mole ratio. The mixture was firstly calcinated at 450 °C for 5 h, then calcinated at 850 °C for 12 h in air and cooled naturally.

2.2. Laboratory X-ray diffraction and scanning electron microscopy

Powder X-ray diffraction (XRD, D8 Bruker) using Cu-Kα radiation ($\lambda = 1.5405$ Å) was employed to identify the crystalline phase of the synthesized materials. XRD data were collected in the scan range (2θ) of 10–90°. The particle size and morphology were measured by scanning electron microscopy (SEM, Hitachi-S4800) with an accelerating voltage of 10 kV.

2.3. Neutron total scattering

Neutron total scattering data were collected at the NOMAD beamline at the Spallation Neutron Source (SNS) at Oak Ridge National Laboratory (ORNL). About 0.1–0.2 g powder samples (carbon, pristine sample with/without carbon, samples charged to 4.4 V, charged to 4.8 V and discharged to 2.5 V) were loaded into 3 mm quartz capillaries and sealed using epoxy in a He filled glove box. Two 1 h scans were collected for each powder sample and they were summed together to improve the statistics. The obtained diffraction data were normalized against a vanadium rod, the background was subtracted, and the total scattering structure factor S(Q) data after subtract the carbon background were transformed to the reduced pair distribution function data G(r) using the specific IDL codes developed for the NOMAD instrument [26]. The Q range used for the Fourier transfer is 0.2 $Å^{-1}$ to 28 $Å^{-1}$ for the sample charged to 4.8 V and 0.2 $Å^{-1}$ to 30 $Å^{-1}$ for the rest. For Bragg diffraction data, the conversion from time-of-flight to d-spacing was done using 2nd order polynomial parameters ($TOF = d_0 + dfc*d + dfa*d^2$) calibrated from a NIST Si 640e standard sample. During the refinement, d_0 and dfc were fixed to the values refined from Si standard while *dfa* was allowed to vary to account for the sample displacement. The diffraction peak shapes were primarily modeled using a pseudo-Voigt function, with an additional convolution to model the moderator related peak shape for TOF neutron diffraction data. For PDF data, small box (unit-cell based) refinements were carried out in the TOPAS software (version 6) [27]. The instrumental parameters Q_{damp} and Q_{broad} were set to be 0.022 $Å^{-1}$ and 0.026 $Å^{-2}$ based on the refinement of a standard Si sample [28].

2.4. Hard X-ray absorption spectroscopy (hXAS)

Mn, Co, Ni K-edge hard X-ray absorption spectroscopy (XAS) spectra were collected in transmission mode at beamline 14BLW1 of Shanghai Synchrotron Radiation Facility (SSRL, China). The X-ray absorption near edge structure (XANES) spectra were processed using the Athena software package (spectra normalization and background subtraction by AUTOBK algorithm).

2.5. Soft X-ray absorption spectroscopy (sXAS) and resonant inelastic X-ray scattering (RIXS)

The total electron yield (TEY) & total fluorescence yield (TFY) XAS spectra and X-ray RIXS maps were collected in the newly commissioned ultra-high efficiency iRIXS end station at Beamline 8.0.1 of the ALS [29]. Before measurements, all samples were processed in glove box with high purity Ar environment. Then a specially designed sample transfer kit was used to transfer the mounted samples into the experimental vacuum chamber, avoiding any airexposure [30]. Radiation damage was monitored by multiple scans of XAS and was considered negligible for these samples. The electrode sample surfaces were mounted at 45° to the incident X-ray beam, while outgoing photon direction along the RIXS spectrograph is 90°. More technical details about RIXS measurements are suggested to refer to the corresponding literatures [31].

2.6. Electrochemical tests

The electrochemical characterizations were performed using CR2025 coin cells. To prepare the positive electrode, the active material was mixed with 10% of carbon black and 10% of polyvinylidene fluoride (PVDF) in N-methyl pyrrolidinone (NMP) solvent until slurry was obtained. The blended slurries were pasted onto an aluminum current collector, followed by cutting to 8 mm in diameter and drying at 120 °C in vacuum for 10 h. The test cell consisted of the positive electrode and lithium foil negative electrode separated by a porous polypropylene film, and 1 mol/L $LiPF_6$ in ethylene (EC) and dimethyl carbonate (DMC) (1:1 in volume) as the electrolyte. The charge and discharge tests were carried out using a Land CT2001A battery test system (Wuhan, PR China) in a voltage range of 2.0–4.8 V at the current density of 20 mA/g at temperature of 25 °C.

2.7. Calculation methods

First-principles calculations were performed in the spin polarized GGA + U approximations to the Density Functional Theory (DFT) as implemented in the Vienna ab initio simulation package [32]. The Hubbard U correction was introduced to describe the effect of localized d electrons of the transition-metal ions. The same effective U value as applied in our previous report was introduced to describe the effect of localized d electrons of the transition-metal ions [33]. The Brillouin zone was sampled with a dense k-points mesh by Gamma packing. A model supercell was used containing 14 Li (2 within the transition metal layer), 3 Ni, 7 Mn and 24 O, corresponding to a stoichiometry of Li $[Li_{2/12}Ni_{3/12}Mn_{7/12}]O_2$. Specific lithium concentration $Li_{14/14}$, $Li_{10/14}$,

$Li_{4/14}$, and $Li_{2/14}$ were selected to represent pristine, 4.4 V, 4.5 V, 4.8 V state of charge, respectively. To obtain the ground state for different lithium vacancies configurations, the atomic positions and cell parameters were fully relaxed. The TM oxidation state is inferred from the calculated magnetization result.

The crystal overlap population scheme of the LOBSTER method (version 2.2.1) was employed to study bonding and chemical interaction properties [34]. The pbeVaspFit2015 basis set was used for the Li, Ni, Mn, and O atoms [35]. The basic functions (localized orbitals) employed in the reconstruction of the PAW wave functions are the following: Li: 1s, 2s; Ni: 4s, 3p, 3d; Mn: 4s, 3p, 3d; O: 2s, 2p. The "completeness" of the above basis functions in representing the valence electronic configuration of the POTCAR files used in the VASP calculations was verified with a small absolute charge spilling value of 0.56%–0.83%. In order to match the number of bands in the VASP calculations with the number of orbitals used in the LOBSTER projection scheme, the VASP input parameter NBANDS was set to 216 for all model systems [36]. Symmetry was switched off (ISYM = −1) for all VASP calculations. Crystal orbital overlap population (COOP) is very powerful in understanding chemical bonding by showing the bonding (COOP>0), and antibonding (COOP<0) character of each studied chemical bonds [37]. The COOP was calculated for several interactions within the bulk material: Ni–O, Mn–O, and O–O inter-planar and intra-planar interactions. For the O–O COOP interactions, significant changes in bonding take place upon de-lithiation within the energy range of −0.5 eV–1.5 eV (relative to the Fermi level). In order to examine and visualize the changes in O–O bonding properties upon delithiation, we applied the PARCHG method to calculate the partial (band decomposed) charge density within the −0.5 eV–1.5 eV energy window.

2.8. Summary of literature

In order to understand the effect of various TM ions contents on the initial Coulombic efficiency and the initial charge capacity provided by the lattice oxygen redox in LRLO materials, the electrochemical performance of some typical literatures is compared and summarized. For the selected $Li[Li_{(2x-1)}Mn_xNi_{(2-3x)}]O_2$ materials [38–41], the atomic ratio between high-valence cations (i.e., Mn^{4+}) and low-valence cations (i.e., Ni^{2+} and Li^+) on the TM layer is not very suitable for the formation of perfect local honeycomb structure. For the selected $Li[Li_{(x-1/3)}Mn_x(Ni\text{-}Co)_{(2/3-x)}]O_2$ materials [42–47], the atomic ratio between high-valence cations (i.e., Mn^{4+} and Co^{3+}) and low-valence cations (i.e., Ni^{2+} and Li^+) on the TM layer is 2:1, which is favorable for the formation of perfect local honeycomb structure.

3. Results

3.1. Electrochemistry and pristine structure

The as-prepared LMR-NMC model compound is found to be a pure phase with spherical-shaped particles (Fig. S1). As shown in Fig. 1a, upon the initial charging process, a high capacity of ~320 mA h/g is obtained, equivalent to 1.02 Li extraction (1.02 charge transfer). Then an excellent reversible capacity of ~288 mA h/g is achieved upon the subsequent charge-discharge process, corresponding to 0.92 Li re-insertion (0.92 charge transfer). This sufficient extraction and re-insertion of Li can bring as much charge transfer as possible which is achieved by the cumulative redox of TM and lattice oxygen. Since the capacity provided by the charge compensation of TM is limited (the maximum amount is 0.39 e^-),

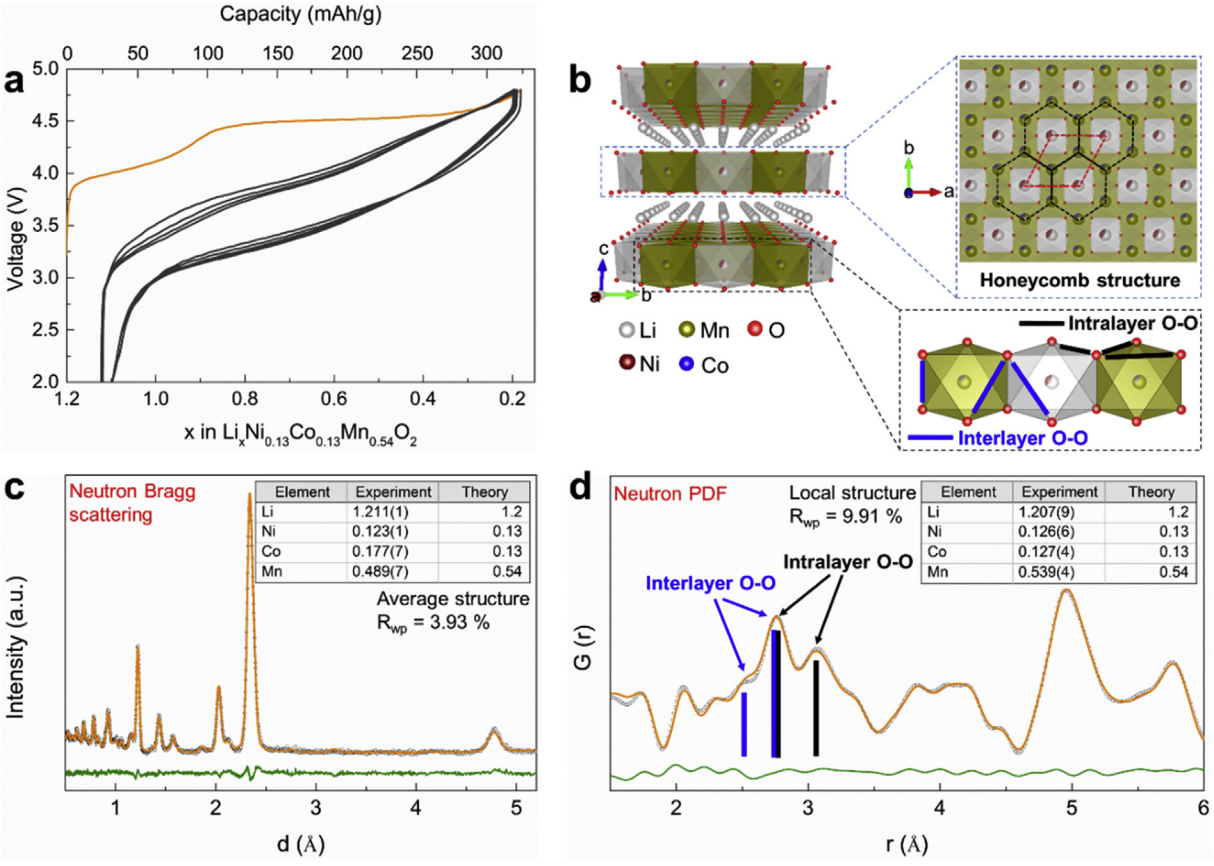

Fig. 1. Electrochemical performance and crystal structure analysis for the pristine LMR-NMC. (a) Charge-discharge curves (5 cycles) for LMR-NMC at 20 mA/g. (b) Crystal structure for the pristine LMR-NMC, short-range honeycomb ordered structure of cations in the *ab*-plane and the schematic of interlayer and intralayer O–O pair distances with corresponding PDF peaks labeled in (d). (c, d) Refinement results using neutron Bragg diffraction data (2θ = 31° bank) (c) and neutron PDF (d), inset table shows the comparison of refined composition and nominal composition. Refer to Fig. S2 and Tables S1–3 for more details.

the rest of the charge compensation (0.63 e^-) is attributed to the l-OR. In this regard, the selected LMR-NMC model in this research is ideal for the study of the l-OR mechanism in detail.

It was previously reported that cations are not randomly distributed in the TM layer of this compound [48]. The cations with higher oxidation states ($Mn^{4+}$and Co^{3+}) prefer to be surrounded by lower valence cations (Ni^{2+} and Li^{+}) to minimize the electrostatic energy. Therefore, considering the atomic ratio of 1:2 between the lower-valence cations and the higher-valence cations on TM layers, it is very likely that they will form (in the *ab*-plane) short-range honeycomb ordering (Fig. 1b). This assessment is confirmed by the excellent fit of local PDF (1–6 Å) using the honeycomb ordered model (*S.G. C2/m*, Fig. 1d and Table S1). The saw-tooth-like diffuse scattering peak (or Warren peak) between 20° and 30° (2θ) in the XRD pattern (Fig. S1) indicates the presence of stacking faults of honeycomb-ordered layers along the *c*-axis, a common phenomenon for this type of material. This is also in good agreement with the different cation occupancies refined from neutron Bragg diffraction data (long-range structure) or intermediate range (6–40 Å) neutron PDF data relative to those refined from local nPDF data (short-range structure), as can be seen in the inset of Fig. 1c, d, Fig. S2 and Tables S1–3. The cation occupancies refined from local PDF (1–6 Å) are consistent with the nominal composition ($Li[Li_{0.2}Ni_{0.13}Mn_{0.54}Co_{0.13}]O_2$) while the values refined from Bragg diffraction data and intermediate range PDF varies substantially, indicating that honeycomb ordered TM layers are not perfectly ordered along the *c*-axis direction. Two drastically different TM interlayer O–O pair distances are refined from local nPDF data, one with the shorter distance around 2.50–2.60 Å, and the other with the longer distance around 2.70–2.75 Å, as can be seen in Fig. 1b, d.

3.2. Charge compensation mechanism

The charge compensation process in the LMR-NMC oxide upon cycling is investigated using joint hard and soft X-ray absorption spectroscopy (XAS). As shown in Fig. 2b, the evolution results of Ni, Co and Mn K-edge XANES spectra upon the first cycling process are consistent with previous reports [13]. Specifically, during the charging process before 4.4 V, the charge compensation in the LMR-NMC is mainly provided by the oxidation of Ni and Co; During the subsequent charging process to 4.8 V, the charge compensation is mainly provided by the oxidation of lattice oxygen to balance the extra extracted Li. Fig. 2c displays the significantly changed O K-edge pre-edge of a series of electrodes at different electrochemical states. The intensity of the pre-edge features between 527 and 535 eV increases upon charging, which has been used as an indication of oxygen redox in previous works. However, it has been clarified that the O–K pre-edge intensity increase is due to the enhanced TM 3d-O 2p hybridization from the high-valence TMs upon charging [49], which is observed for almost all battery cathodes including $LiFePO_4$ with no oxygen redox [50]. Nonetheless, our data indicate that there is likely a new feature emerging around 531 eV at the fully charged state (orange spectrum in Fig. 2c), which matches the absorption energy of oxidized oxygen species [51].

In order to clarify and confirm the l-OR mechanism, we employ the full energy range mapping of resonant inelastic X-ray scattering (mRIXS) of the O–K edge. Technically, mRIXS could further resolve the single data spot of XAS into an intensity distribution plot upon the emission energy of the fluorescence photons. This allows us to distinguish the oxygen redox signals from other dominating contributions through a characteristic mRIXS feature at 523.5 eV emission energy (white arrow in Fig. 2d) [24,49]. As shown in Fig. 2d, both charged and discharged electrodes display broad mRIXS features along 525 eV emission energies. These features are typical O^{2-} features of TM oxides from the TM 3d-O 2p hybridizations (below 535 eV excitation energy) and TM-4sp involved O 2p bands. Notably, other than the 525 eV emission energy mRIXS features in the charged state, a clear feature at 523.5 eV emerges at the 4.8 V-charged state. This feature (523.5 eV emission energy) fingerprints the oxidized oxygen that manifests itself exclusively from sub-surface oxygen [52] and only if there is the l-OR involved in electrodes [53], thus providing the ultimate verification of the l-OR activity in our model

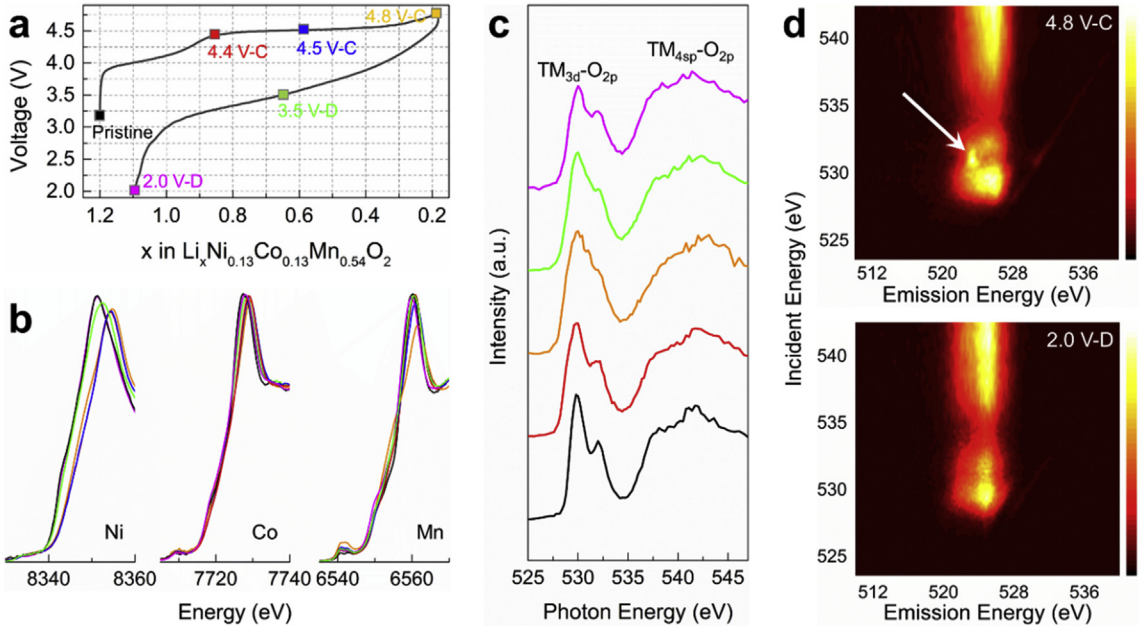

Fig. 2. Evolution of the TM K-edge, O K-edge XAS and RIXS upon the electrochemical cycling process. (a) The first cycle curve for LMR-NMC. (b) *Ex situ* Ni K-edge, Co K-edge, and Mn K-edge XANES spectra at different electrochemical states indicated in (a). (c) *Ex situ* sXAS spectra (Fluorescence yield mode) of the LMR-NMC at different electrochemical states indicated in (a). (d) RIXS maps of the LMR-NMC at the 4.8 V-charged and 2.0 V-discharged states during the first cycle. The unique emission signature at oxidation state indicated by the white arrow supports an electronic restructuring associated with O redox. Refer to Figs. S3 and 4 for more details.

compound.

3.3. Local and average structure evolution associated with the l-OR

Ex situ nPDF results collected at different charge-discharge states are shown in Fig. 3c. It can be seen from the PDF pattern that the location and intensity of the shoulder at the left of the main O–O peak (corresponding to short O–O pairs) located at about 2.55 Å changes slightly until the LMR-NMC is charged to 4.4 V. This indicates the local oxygen environment is mostly maintained during TM redox process. Notably, a drastic increase of this shoulder peak intensity is observed when the LMR-NMC is charged from 4.4 V to 4.8 V. For a specific atomic pair, the relative intensity of the PDF peak is associated with the abundance of these pairs. Therefore, the dramatic increase in the intensity of the PDF peak at 2.30–2.60 Å manifests the formation of large amounts of short O–O pairs (or distorted oxygen lattice).

According to the *ex situ* XAS and RIXS results, Ni and Co ions mainly participate in the charge-compensation during the charging process from the pristine state to the 4.4 V charged state while lattice oxygen ions dominate the charge compensation during the subsequent charging process from 4.4 V to 4.8 V. The asymmetrical variation of the local PDF peak located at around 2.0 Å upon cycling also agrees well with the above charging compensation process (Fig. 3c). The increased number of the short O–O pair (<2.60 Å) is thus not caused by the oxidation of TM ions, but directly correlated with the charge-compensation of the l-OR. This observation is further supported by quantitative structure refinement using local nPDF. The percentage variation in the amounts of short O–O pairs at different electrochemical states in the local and average structure is shown in Fig. 3d and e, respectively. Notably, the change of short O–O pairs cannot be detected accurately by quantitatively analyzing the average structure using Bragg diffraction data (Fig. 3e), indicating the l-OR is likely to be a local or short-range phenomenon. This also explains why this phenomenon has evaded previous detection by more typical diffraction techniques (e.g., X-ray or neutron Bragg diffraction). Upon the discharging process, the increased short O–O pairs disappear (Fig. 3d), meaning that the local structure adaption (or distortion) accompanying

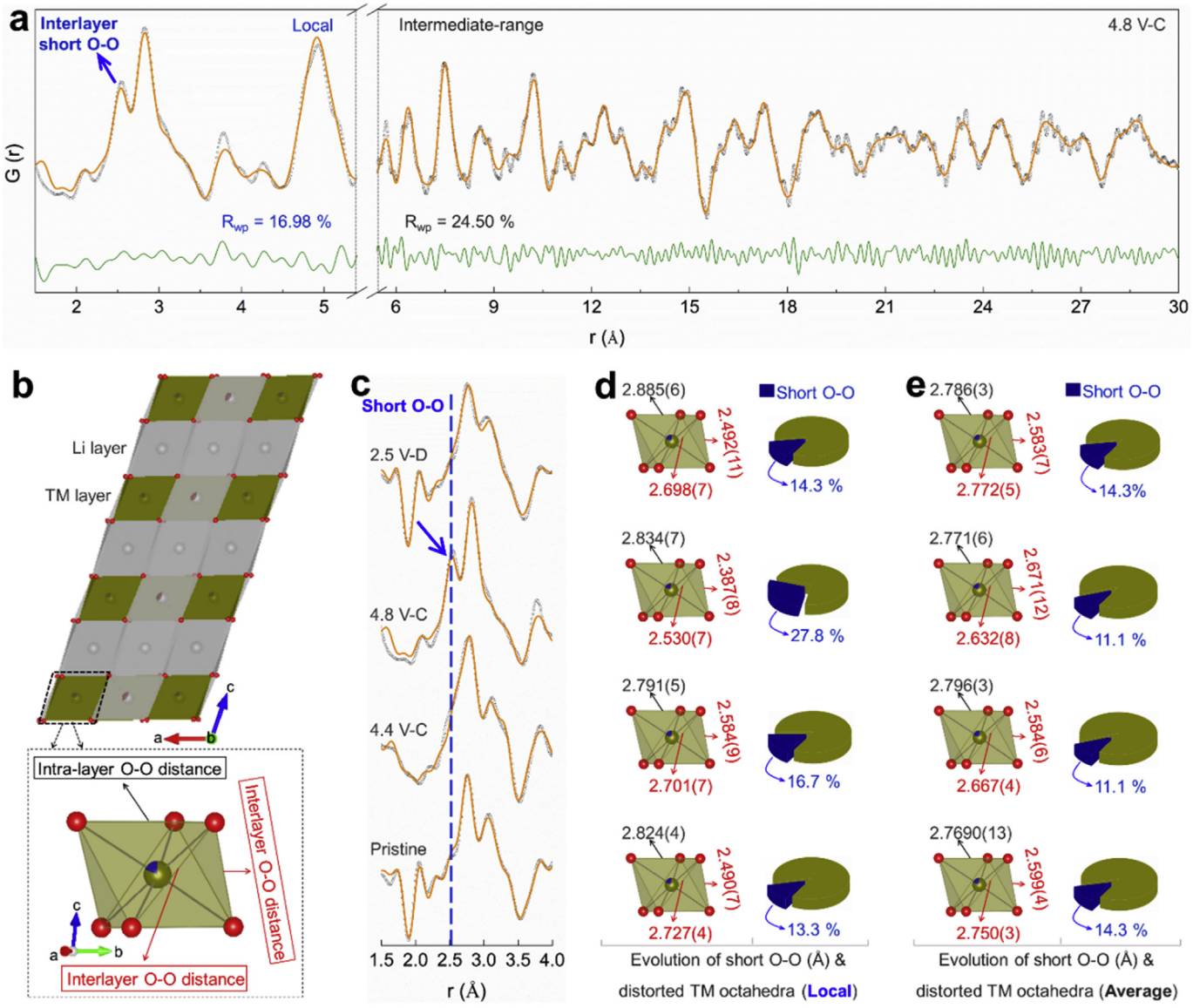

Fig. 3. Evolution of the local and average crystal structure of LMR-NMC upon the initial cycling process. (a) Refinement results using local (left panel) and intermediate-range (right panel) neutron PDF at 4.8 V charged state. (b) Schematic of interlayer and intralayer O–O distance in the TM octahedra. (c) Comparison of the *ex situ* nPDF results of LMR-NMC collected at different charge-discharged states. (d, e) The variation in percentage of short O–O pairs and distorted TMO_6 octahedra in local (d) and average (e) structure during the first cycle. The percentage of short O–O pairs is the ratio between the number of O–O pairs distance less than ~2.6 Å and the number of O–O pairs distance less than ~3.0 Å. More details can be found in Figs. S5–14, Supplementary Tables S4–12.

the l-OR is reversible.

In addition, it is worth noting that although there is an obvious local structure distortion upon the l-OR process, the global layered structure of the LMR-NMC compound is well preserved, which, in turn, is favorable for the stable and reversible l-OR (Fig. 3c). Meanwhile, it is found that only the interlayer O–O distance is decreased while the intralayer O–O distance is well maintained during the l-OR process (Figs. S12–14), suggesting that the structural response to the l-OR activity is highly selective. The origin of this selective structural response and stable/reversible lattice structure evolution upon the l-OR is discussed in the following section.

4. Discussion

4.1. Origin of the stable and reversible l-OR

The Li–O–Li configuration model with unhybridized O 2p state (Figs. S16 and 17) proposed by Ceder et al. successfully explained the observed l-OR activity in a variety of LRLO materials [10]. However, there are still a few puzzling questions regarding the l-OR behavior including the selective (non-random) decrease of O–O distance in the oxidized (delithiated) materials observed in this work and elsewhere (e.g., Li_2IrO_3 [11], P3-type $Na_{0.6}Li_{0.2}Mn_{0.8}O_2$ [54]), and the origin of the stable and reversible l-OR (e.g., the high initial Coulombic efficiency in LMR-NMC compound).

To better understand these ambiguities, it is worth paying attention to the local coordination environments of the lattice oxygen. There are three different interactions between the oxidized oxygen ions (denoted as O^-) (Fig. 4a and b). Specifically, the first is the interaction between two O^- with parallel unhybridized O 2p orbitals. Potential π-type overlap or π-bonding may form between these two O^- by decreasing the O–O distance. The energy of these isolated O^- is expected to be lowered by O 2p-2p π-type overlapping or (partially) forming the O–O dimer via π-bonding, as illustrated in Fig. 4c. A similar situation could exist for the σ-type overlap. However, it is noteworthy that the (unhybridized) O 2p orbitals have to rotate about 45° toward each other to enable full σ-type overlap or σ-bonding, as illustrated in Fig. 4d. This rotation would result in drastic weakening of the TM-O bonds by decreasing the overlap between TM 3d/4s/4p and O 2p orbitals. Thus, it is very likely that the π-type overlap is preferred relative to the σ-type overlap. Lastly, there shall be no effective orbital overlap between the intralayer O^-, because the corresponding unhybridized O 2p orbitals are non-coplanar (Fig. 4b). Therefore, the intralayer O–O distance is expected to be well-maintained upon the l-OR process. This is fully consistent with the calculation results from COOP using the model system of $Li_{12}[Li_2Ni_3Mn_7]O_{24}$ (or $Li[Li_{1/6}Ni_{1/4}Mn_{7/12}]O_2$). As shown in Fig. 5a and b, a conspicuous increase in the integrated intensity of O–O projected COOP is found upon the delithiation process, which suggests the formation of stronger O–O interaction due to the oxidation of oxygen. Meanwhile, the local O–O COOP plots for Ni and Mn sites prove that the increased O–O interaction in the overall delithiated structure mainly originates from the interlayer O–O interaction (Fig. 5c, d and Figs. S23 and 24). The above analysis can well explain the unique structural response to the oxidation of oxygen observed experimentally. Specifically, other than the effect of electrostatic repulsion [55], the selective decrease of O–O distance (interlayer rather than intralayer) mainly originates from the distinct nature of the potential O–O chemical bonds within the octahedral environment.

It is also worth noting that the shortest O–O distance (~2.39 Å) observed in the 4.8 V charged sample is much longer than the real peroxide (O_2^{2-}) bond length (~1.5 Å) [56], but similar to the peroxo-like O–O dimer (in which σ-type overlap dominates) distance (~2.45 Å) observed in 5d TM LRLO [11]. As mentioned above (Fig. 4d), a rotation

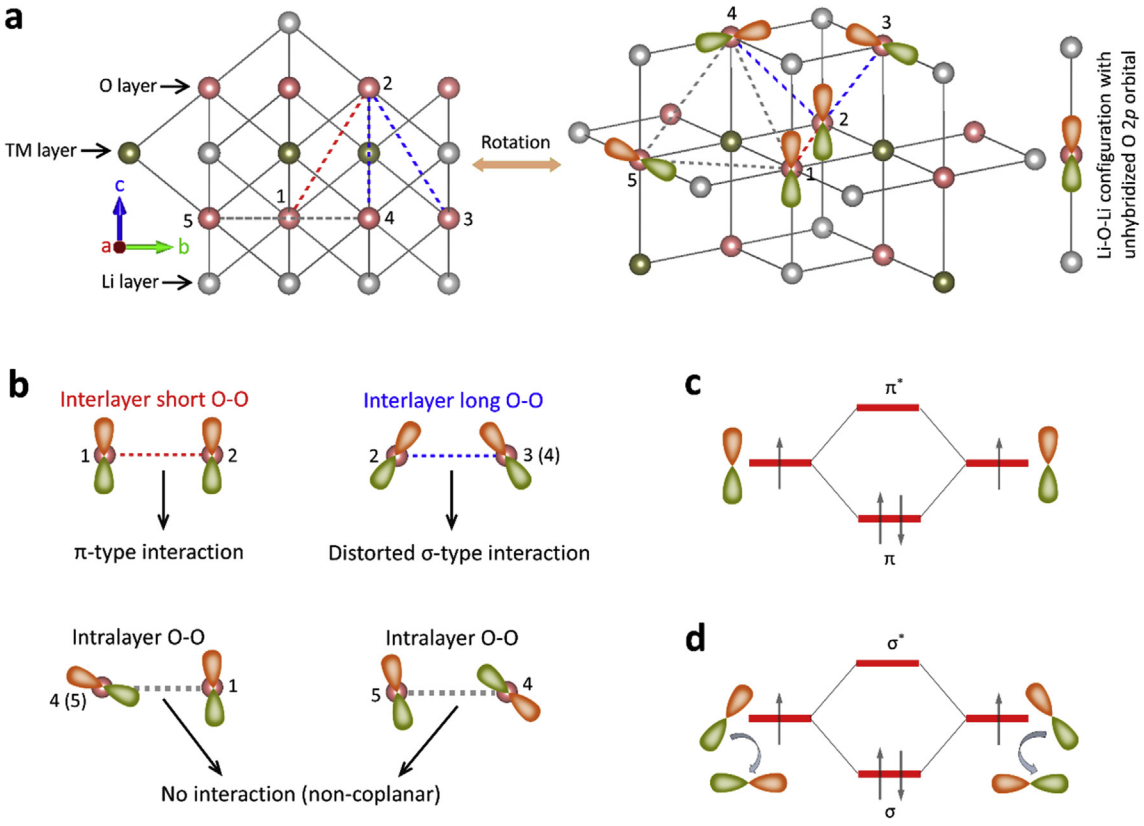

Fig. 4. Schematic of the interactions between oxidized lattice oxygen ions in Li-rich layered oxides. (a) Crystal structure with unhybridized O 2p orbitals along Li–O–Li configurations for the Li-rich layered oxides. (b) Three different interactions between the oxidized oxygen ions, potential π-type or σ-type interactions between the interlayer oxidized oxygen ions, no interaction between the intralayer oxidized oxygen ions due to the non-coplanar unhybridized O 2p orbitals. (c, d) Formation process of π-type overlap or π-bond (c) and full σ-type overlap or σ-bond (d) between two unhybridized O 2p orbitals. See also Fig. S18.

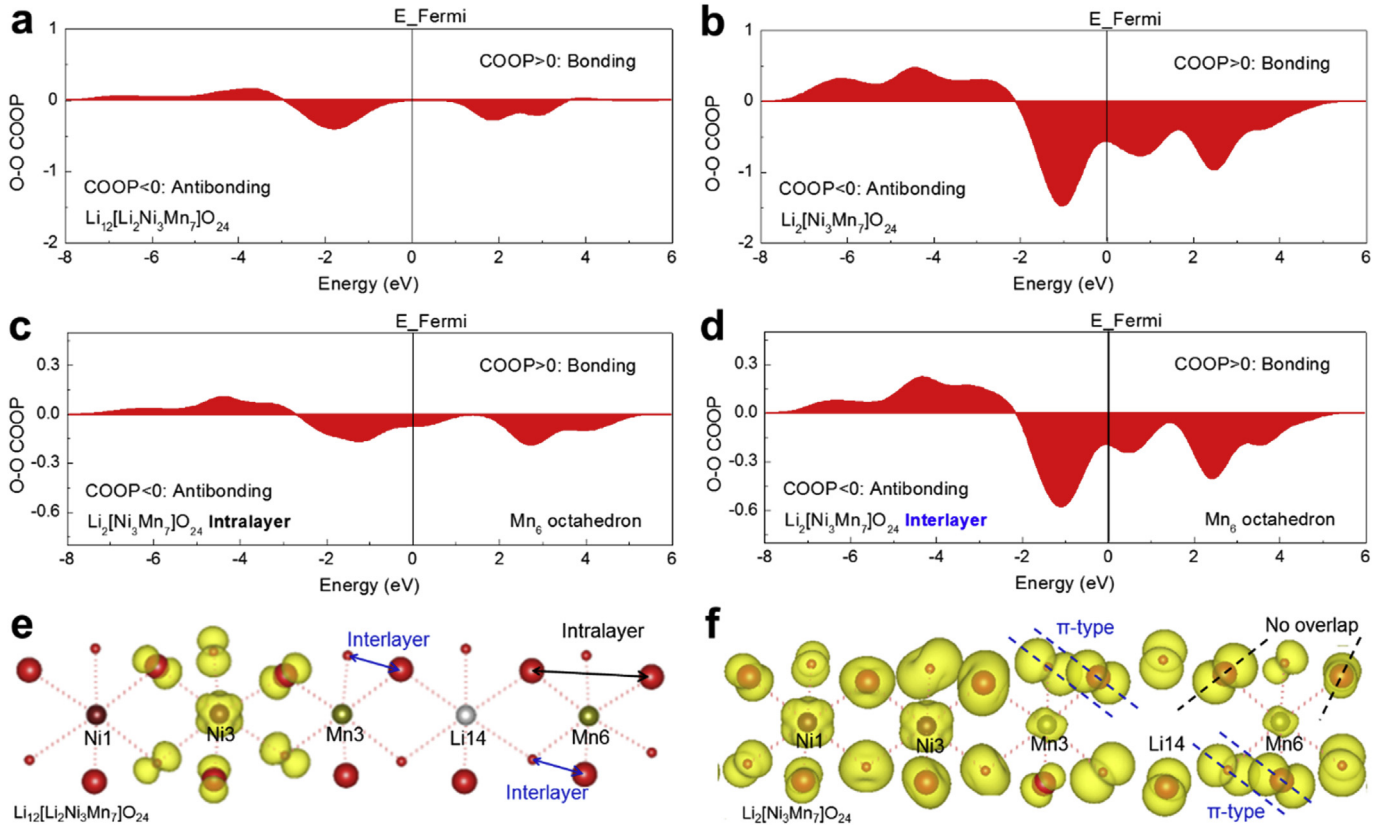

Fig. 5. Evolution of O–O chemical bonding nature of $Li_{12}[Li_2Ni_3Mn_7]O_{24}$ based on density functional theory (DFT) calculations. (a, b) Projected (shaded area) COOP using Lobster program for O–O bonding in $Li_{12}[Li_2Ni_3Mn_7]O_{24}$ (a) and $Li_2[Ni_3Mn_7]O_{24}$ (b). (c, d) Comparison of the intralayer (c) and interlayer (d) O–O COOP for Mn_6 site in $Li_2[Ni_3Mn_7]O_{24}$. (e, f) The electron density isosurface contour plots in energy range (−0.5 eV, 1.5 eV) relative to the Fermi level for $Li_{12}[Li_2Ni_3Mn_7]O_{24}$ (e) and $Li_2[Ni_3Mn_7]O_{24}$ (f). The O–O bonding COOP plots in (a, b) include all the O–O pairs within bonding distance (2.3 Å, 2.6 Å) and COOP plots for Mn_6 site in (c, d) include 6 intralayer or interlayer O–O pairs. Refer to Figs. S19–24 for more details.

of the TM-O-TM angle (Fig. S18) must occur for σ-bond or full σ-type overlap formation in this short O–O pair. However, nPDF results suggest that there is no obvious distortion of the TM-O-TM angle upon the oxygen oxidation process (Fig. 3a and Fig. S5). Calculation results of the model compound also indicate that there is no obvious weakening of the TM-O bonding (Fig. S24). This relatively rigid structure effectively prevents the real peroxide or peroxo-like species formation when the oxidized oxygen ions move closer to each other. In addition, we indeed find that the O–O distance associated with the π-type overlap is shorter relative to that with the potential σ-type overlap (Figs. S12–14). Thus, π-type overlap is very likely to dominate the interaction in this short O–O pair, which can essentially lower the energy of the locally distorted structure and thus stabilize the overall l-OR. This localized structure adaption with the π-type O–O overlap not only accommodates the l-OR but also preserves the global layered structure in LRLO materials (Fig. 6a).

4.2. Multi TM species for stable layered structure and reversible l-OR

Taken together, the l-OR will result in the change of electronic coordination environment around oxygen atoms, which will then lead to the crystal structure adaption (for example the local distorted oxygen lattice in this work). As discussed above, the local structure distortion (or the shortening of the local interlayer O–O distance) will compete with the maintenance of the rigid layered structure upon the l-OR process. The excessive structure distortion would not only destroy the overall layered structure but also inevitably lead to O_2 recombination as well as irreversible TM migration/phase transition [57], thus resulting in a series of electrochemical issues for LRLO materials, such as voltage fade/hysteresis, capacity degradation, etc. Therefore, to rein these unfavorable electrochemical results and achieve reversible high energy density, it is necessary to limit the lattice distortion in a localized-structure range.

It is found that the adaption of oxygen lattice is highly dependent on the nature of TM species. For instance, the decrease of O–O distance tends to occur in Mn^{4+} octahedron rather than in Ni^{4+} octahedron (Fig. S15). Calculation results also indicate that the O–O 2p orbital overlap (π-type overlap) is more likely to occur in Mn^{4+} compared with Ni^{4+} (Fig. 5f). The phenomenon is ascribed to the different covalency between Mn–O and Ni–O interactions. Generally, the TM-O-TM angle (or TM-O bonding) will be more rigid for cations with stronger covalency (e.g., Ni^{4+}) relative to those with stronger ionicity (e.g., Mn^{4+}) [10]. Thus, we can utilize multi TM species with different degrees of TM-O bonding covalency to tune the oxygen lattice adaptability. Specifically, a localized crystal structure (e.g., honeycomb structure) can be constructed by multi TM species to achieve both the flexibility (to accommodate the l-OR) and rigidity (to maintain the global layered structure) of the oxygen lattice in LRLO materials (Fig. 6a).

This assessment is confirmed by literature reported results (Fig. 6b and c) as well as our experimental observations (Fig. 6b). The initial charge capacity provided by the l-OR (iCC-OR) increase with the content increase of Mn ions (Fig. 6b and c, top panel), other than the effect of Li-ions content in the TM layer. This can well be ascribed to the reason that high-ionicity Mn ions can better accommodate the l-OR and thereby facilitate the release of initial charge capacity provided by the l-OR. However, to achieve the high initial Coulombic efficiency (iCE, which is closely correlated with the reversibility of the l-OR), a coordination of a certain amount of highly-covalent TM ions (e.g., Ni ions) in the LRLO material is necessary (Fig. 6b and c, bottom panel). In addition, it is worth noting that both relatively high iCC-OR and high iCC can only be

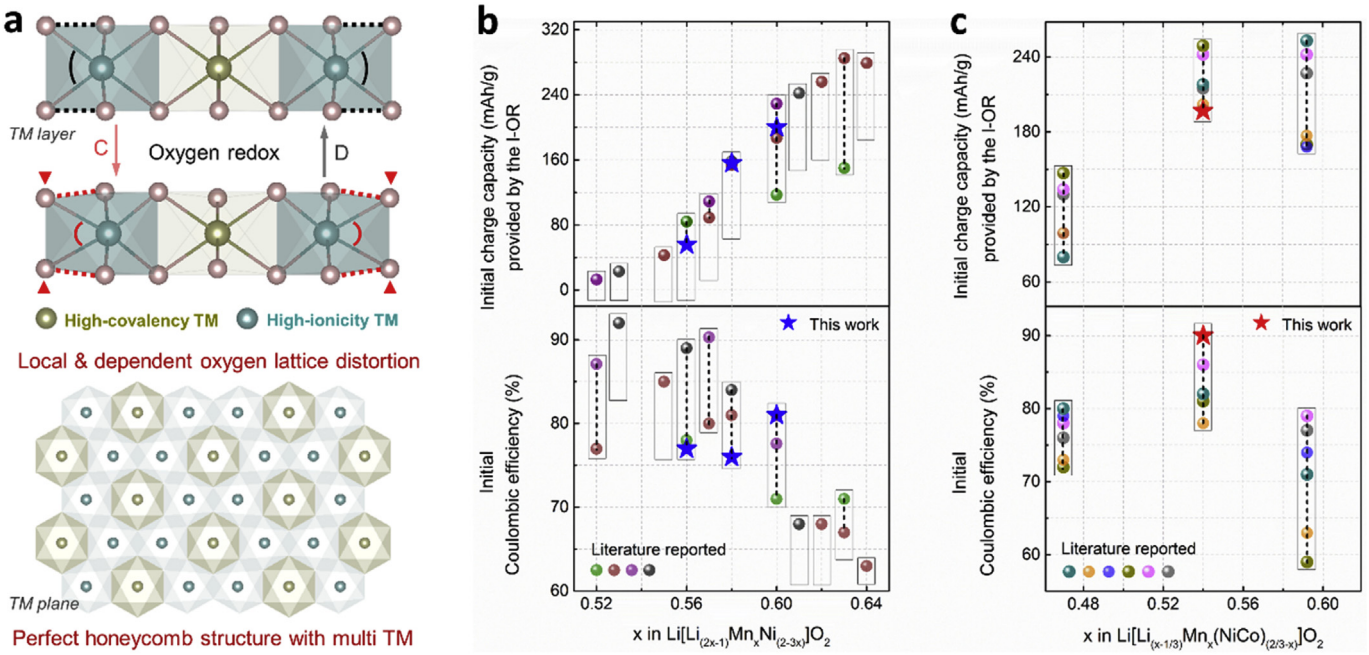

Fig. 6. (a) Schematic for the localized and dependent (i.e., closely correlated with the TM species). distorted oxygen lattice upon the cycling process, a perfect local honeycomb structure with multi TM is needed to accommodate the l-OR while preserve the global layered structure. The effect of various TM contents on the initial Coulombic efficiency (iCE) and the initial charge capacity provided by the l-OR (iCC-OR) in LRLO materials: (b) the variation results of the iCE and the iCC-OR with the contents of Mn and Ni ions on the TM layer in $Li[Li_{(2x-1)}Mn_xNi_{(2-3x)}]O_2$ materials, our experimental results are highlighted using blue star in the plot; (c) the variation results of the iCE and the iCC-OR with the contents of Mn and Ni&Co ions on the TM layer in $Li[Li_{(x-1/3)}Mn_x(NiCo)_{(2/3-x)}]O_2$ materials, in which the red star represents the LMR-NMC model compound in this work. The atomic ratio between high-valence cations (i.e., Mn^{4+}, Co^{3+}) and low-valence cations (i.e., Ni^{2+}, Li^{+}) on the TM layer in (c) is 2:1 which is favorable for the formation of perfect local honeycomb structure. The corresponding references in the plot can be found in the summary literature section. (For interpretation of the references to colour in this figure legend, the reader is referred to the Web version of this article.)

obtained in LRLO materials with perfect local honeycomb structure (in which the atomic ratio between higher-valence cations (i.e., Mn^{4+}, Co^{3+}) and lower-valence cations (i.e., Ni^{2+}, Li^{+}) in the TM layer is 2:1, Fig. 6c). This is because that the perfect local ordered structure with variant-covalency TM ions intrinsically define the adaption of oxygen lattice in a localized range, which not only accommodate the l-OR activity but also well preserve the global layered structure in LRLO materials. The above finding is also fully consistent with our experimental observations (high iCE in Fig. 1a and reversible local structure distortion in Fig. 3c) in the LMR-NMC model compound which is comprised of three different TM cations (Fig. 6c) with perfect local honeycomb structure (Fig. 1b). Therefore, to obtain the stable layered structure and enable reversible l-OR activity, LRLO material with both rigid and flexible oxygen lattice can be designed by introducing multi TM species with the optimal atomic ratio.

5. Conclusion

In summary, a local distorted oxygen lattice structure induced by the l-OR in LMR-NMC was for the first time detected through the neutron PDF analysis. This localized-distortion lattice reduces the energy of the model system accommodating the l-OR activity while preserves the global layered structure. Crucially, by employing theoretical calculations, we revealed that the distortion of oxygen lattice is highly selective. The oxygen lattice with a stronger-ionicity TM-O chemical bond is more likely to distort than that with a stronger-covalency environment. These of importance findings not only deepen the understanding of l-OR mechanisms but also present an illuminating tenet that the TM-O chemical bond as well as the local crystal structure can be tuned to achieve both rigidity and flexibility of the crystal structure in LRLO materials, thus achieving their reversible high energy density with stable l-OR.

Acknowledgements

The work done at Institute of Physics, Chinese Academy of Sciences was supported by funding from National Key R&D Program of China (2016YFB0100100), National Materials Genome Project (2016YFB0100106), NSFC (Grant No. 11675255, 51502334, 51822211) and "Thousand Talents Program for Young Scientists". The work done at UCSD was supported by the Assistant Secretary for Energy Efficiency and Renewable Energy, Office of Vehicle Technologies of the U.S. Department of Energy under Contract DE-AC02-05CH11231, Subcontract 7073923, under the Advanced Battery Materials Research (BMR) Program. Research conducted at the NOMAD beamline at ORNL's SNS was sponsored by the Scientific User Facilities Division, Office of Basic Sciences, USDOE. J.L. and K.P are partially supported by U.S. DOE, Office of Science, Office of Basic Energy Sciences, Early Career Research Program award KC040602, under contract number DE-AC05-00OR22725. The work at BNL were supported by the Assistant Secretary for Energy Efficiency and Renewable Energy, Vehicle Technology Office of the U.S. DOE through the BMR Program, including Battery 500 Consortium under contract DE-SC0012704. The authors are very indebted to Prof. Yonggao Xia (Ningbo Institute of Materials Technology and Engineering, Chinese Academy of Sciences) for the insightful discussion on this paper. sXAS data were collected at beamline 8.0.1 of the ALS, which is supported by the Director, Office of Science, Office of Basic Energy Sciences, of the U.S. DOE under Contract No. DE-AC02-05CH11231. We thank the help from beamline BL14W1 at SSRL, China. This manuscript has been authored by UT-Battelle, LLC under Contract No. DE-AC05-00OR22725 with the U.S. DOE. The United States Government retains and the publisher, by accepting the article for publication, acknowledges that the United States Government retains a non-exclusive, paid-up, irrevocable, worldwide license to publish or reproduce the published form of this manuscript, or allow others to do so, for United States Government purposes. The DOE

will provide public access to these results of federally sponsored research in accordance with the DOE Public Access Plan.

Appendix A. Supplementary data

Supplementary data to this article can be found online at https://doi.org/10.1016/j.ensm.2019.07.032.

References

[1] K. Mizushima, P.C. Jones, P.J. Wiseman, J.B. Goodenough, Li_xCoO_2 (0 < x < -1): a new cathode material for batteries of high energy density, Mater. Res. Bull. 15 (1980) 783–789.

[2] T. Ohzuku, A. Ueda, M. Nagayama, Y. Iwakoshi, H. Komori, Comparative study of $LiCoO_2$, $LiNi_{1/2}Co_{1/2}O_2$ and $LiNiO_2$ for 4 volt secondary lithium cells, Electrochim. Acta 38 (1993) 1159–1167.

[3] Z.H. Lu, D.D. MacNeil, J.R. Dahn, Layered $LiNi_xCo_{1-2x}Mn_xO_2$ cathode materials for lithium-ion batteries, Electrochem. Solid State Lett. 4 (2001) A200–A203.

[4] K.S. Kang, Y.S. Meng, J. Breger, C.P. Grey, G. Ceder, Electrodes with high power and high capacity for rechargeable lithium batteries, Science 311 (2006) 977–980.

[5] J. Liang, L. Wen, X. Yu, F. Li, H.-M. Cheng, Cathode materials: a key challenge for lithiumion batteries, Energy Storage Mater 14 (2018) A1–A3.

[6] J.-L. Shi, D.-D. Xiao, M. Ge, X. Yu, Y. Chu, X. Huang, X.-D. Zhang, Y.-X. Yin, X.-Q. Yang, Y.-G. Guo, L. Gu, L.-J. Wan, High-capacity cathode material with high voltage for Li-ion batteries, Adv. Mater. 30 (2018).

[7] Y. Zuo, B. Li, N. Jiang, W. Chu, H. Zhang, R. Zou, D. Xia, A high-capacity O2-type Li-rich cathode material with a single-layer Li_2MnO_3 superstructure, Adv. Mater. 30 (2018).

[8] M.S. Whittingham, Ultimate limits to intercalation reactions for lithium batteries, Chem. Rev. 114 (2014) 11414–11443.

[9] K. Luo, M.R. Roberts, R. Hao, N. Guerrini, D.M. Pickup, Y.-S. Liu, K. Edstrom, J. Guo, A.V. Chadwick, L.C. Duda, P.G. Bruce, Charge-compensation in 3d-transition-metal-oxide intercalation cathodes through the generation of localized electron holes on oxygen, Nat. Chem. 8 (2016) 684–691.

[10] D.-H. Seo, J. Lee, A. Urban, R. Malik, S. Kang, G. Ceder, The structural and chemical origin of the oxygen redox activity in layered and cation-disordered Li-excess cathode materials, Nat. Chem. 8 (2016) 692–697.

[11] E. McCalla, A.M. Abakumov, M. Saubanere, D. Foix, E.J. Berg, G. Rousse, M.-L. Doublet, D. Gonbeau, P. Novak, G. Van Tendeloo, R. Dominko, J.-M. Tarascon, Visualization of O-O peroxo-like dimers in high-capacity layered oxides for Li-ion batteries, Science 350 (2015) 1516–1521.

[12] X. Li, Y. Qiao, S. Guo, K. Jiang, M. Ishida, H. Zhou, A new type of Li-rich rock-salt oxide $Li_2Ni_{1/3}Ru_{2/3}O_3$ with reversible anionic redox chemistry, Adv. Mater. 31 (2019).

[13] H. Koga, L. Croguennec, M. Menetrier, P. Mannessiez, F. Weill, C. Delmas, S. Belin, Operando X-ray absorption study of the redox processes involved upon cycling of the Li-rich layered oxide $Li_{1.20}Mn_{0.54}Co_{0.13}Ni_{0.13}O_2$ in Li ion batteries, J. Phys. Chem. C 118 (2014) 5700–5709.

[14] X.-D. Zhang, J.-L. Shi, J.-Y. Liang, Y.-X. Yin, Y.-G. Guo, L.-J. Wan, Structurally modulated Li-rich cathode materials through cooperative cation doping and anion hybridization, Sci. China Chem. 60 (2017) 1554–1560.

[15] X. Li, Y. Qiao, S. Guo, Z. Xu, H. Zhu, X. Zhang, Y. Yuan, P. He, M. Ishida, H. Zhou, Direct visualization of the reversible O^{2-}/O^{-} redox process in Li-rich cathode materials, Adv. Mater. 30 (2018).

[16] E. Zhao, L. He, B. Wang, X. Li, J. Zhang, Y. Wu, J. Chen, S. Zhang, T. Liang, Y. Chen, X. Yu, H. Li, L. Chen, X. Huang, H. Chen, F. Wang, Structural and mechanistic revelations on high capacity cation-disordered Li-rich oxides for rechargeable Li-ion batteries, Energy Storage Mater 16 (2019) 354–363.

[17] F. Ning, H. Shang, B. Li, N. Jiang, R. Zou, D. Xia, Surface thermodynamic stability of Li-rich Li_2MnO_3: effect of defective graphene, Energy Storage Mater (2019), https://doi.org/10.1016/j.ensm.2019.01.004.

[18] A. Singer, M. Zhang, S. Hy, D. Cela, C. Fang, T.A. Wynn, B. Qiu, Y. Xia, Z. Liu, A. Ulvestad, N. Hua, J. Wingert, H. Liu, M. Sprung, A.V. Zozulya, E. Maxey, R. Harder, Y.S. Meng, O.G. Shpyrko, Nucleation of dislocations and their dynamics in layered oxide cathode materials during battery charging, Nat. Energy 3 (2018) 641–647.

[19] E. Hu, X. Yu, R. Lin, X. Bi, J. Lu, S. Bak, K.-W. Nam, H.L. Xin, C. Jaye, D.A. Fischer, K. Amine, X.-Q. Yang, Evolution of redox couples in Li- and Mn-rich cathode materials and mitigation of voltage fade by reducing oxygen release, Nat. Energy 3 (2018) 690–698.

[20] Y. Xie, M. Saubanere, M.L. Doublet, Requirements for reversible extra-capacity in Li-rich layered oxides for Li-ion batteries, Energy Environ. Sci. 10 (2017) 266–274.

[21] J. Hong, W.E. Gent, P. Xiao, K. Lim, D.-H. Seo, J. Wu, P.M. Csernica, C.J. Takacs, D. Nordlund, C.-J. Sun, K.H. Stone, D. Passarello, W. Yang, D. Prendergast, G. Ceder, M.F. Toney, W.C. Chueh, Metal-oxygen decoordination stabilizes anion redox in Li-rich oxides, Nat. Mater. 18 (2019) 256–265.

[22] B. Qiu, M. Zhang, Y. Xia, Z. Liu, Y.S. Meng, Understanding and controlling anionic electrochemical activity in high-capacity oxides for next generation Li-ion batteries, Chem. Mater. 29 (2017) 908–915.

[23] B. Li, D. Xia, Anionic redox in rechargeable lithium batteries, Adv. Mater. 29 (2017).

[24] E. Zhao, Q. Li, F. Meng, J. Liu, J. Wang, L. He, Z. Jiang, Q. Zhang, X. Yu, L. Gu, W. Yang, H. Li, F. Wang, X. Huang, Stabilizing the oxygen lattice and reversible oxygen redox chemistry through structural dimensionality in lithium-rich cathode oxides, Angew. Chem. 58 (2019) 4323–4327.

[25] H. Guo, Z. Wei, K. Jia, B. Qiu, C. Yin, F. Meng, Q. Zhang, L. Gu, S. Han, Y. Liu, H. Zhao, W. Jiang, H. Cui, Y. Xia, Z. Liu, Abundant nanoscale defects to eliminate voltage decay in Li-rich cathode materials, Energy Storage Mater 16 (2019) 220–227.

[26] J. Neuefeind, M. Feygenson, J. Carruth, R. Hoffmann, K.K. Chipley, The nanoscale ordered MAterials diffractometer NOMAD at the spallation neutron Source SNS, Nucl. Instrum. Methods B 287 (2012) 68–75.

[27] A.A. Coelho, P.A. Chater, A. Kern, Fast synthesis and refinement of the atomic pair distribution function, J. Appl. Crystallogr. 48 (2015) 869–875.

[28] C.L. Farrow, P. Juhas, J.W. Liu, D. Bryndin, E.S. Bozin, J. Bloch, T. Proffen, S.J.L. Billinge, PDFfit2 and PDFgui: computer programs for studying nanostructure in crystals, J. Phys-Condens Mat. 19 (2007).

[29] R. Qiao, Q. Li, Z. Zhuo, S. Sallis, O. Fuchs, M. Blum, L. Weinhardt, C. Heske, J. Pepper, M. Jones, A. Brown, A. Spucces, K. Chow, B. Smith, P.-A. Glans, Y. Chen, S. Yan, F. Pan, L.F.J. Piper, J. Denlinger, J. Guo, Z. Hussain, Y.-D. Chuang, W. Yang, High-efficiency in situ resonant inelastic x-ray scattering (iRIXS) endstation at the Advanced Light Source, Rev. Sci. Instrum. 88 (2017).

[30] R. Qiao, T. Chin, S.J. Harris, S. Yan, W. Yang, Spectroscopic fingerprints of valence and spin states in manganese oxides and fluorides, Curr. Appl. Phys. 13 (2013) 544–548.

[31] Y.-D. Chuang, Y.-C. Shao, A. Cruz, K. Hanzel, A. Brown, A. Frano, R. Qiao, B. Smith, E. Domning, S.-W. Huang, L.A. Wray, W.-S. Lee, Z.-X. Shen, T.P. Devereaux, J.-W. Chiou, W.-F. Pong, V.V. Yashchuk, E. Gullikson, R. Reininger, W. Yang, J. Guo, R. Duarte, Z. Hussain, Modular soft x-ray spectrometer for applications in energy sciences and quantum materials, Rev. Sci. Instrum. 88 (2017).

[32] G. Kresse, J. Furthmuller, Efficiency of ab-initio total energy calculations for metals and semiconductors using a plane-wave basis set, Comput. Mater. Sci. 6 (1996) 15–50.

[33] B. Qiu, M. Zhang, L. Wu, J. Wang, Y. Xia, D. Qian, H. Liu, S. Hy, Y. Chen, K. An, Y. Zhu, Z. Liu, Y.S. Meng, Gas-solid interfacial modification of oxygen activity in layered oxide cathodes for lithium-ion batteries, Nat. Commun. 7 (2016).

[34] R. Dronskowski, P.E. Blochl, Crystal orbital Hamilton populations (COHP)-energy-resolved visualization of chemical bonding in solids based on density-functional calculations, J. Phys. Chem. 97 (1993) 8617–8624.

[35] V.L. Deringer, A.L. Tchougreeff, R. Dronskowski, Crystal orbital Hamilton population (COHP) analysis as projected from plane-wave basis sets, J. Phys. Chem. A 115 (2011) 5461–5466.

[36] S. Maintz, V.L. Deringer, A.L. Tchougreeff, R. Dronskowski, Analytic projection from plane-wave and PAW wavefunctions and application to chemical-bonding analysis in solids, J. Comput. Chem. 34 (2013) 2557–2567.

[37] M. Saubanere, E. McCalla, J.M. Tarascon, M.L. Doublet, The intriguing question of anionic redox in high-energy density cathodes for Li-ion batteries, Energy Environ. Sci. 9 (2016) 984–991.

[38] J.R. Croy, K.G. Gallagher, M. Balasubramanian, B.R. Long, M.M. Thackeray, Quantifying hysteresis and voltage fade in $xLi_2MnO_3{\cdot}(1\text{-}x)LiMn_{0.5}Ni_{0.5}O_2$ electrodes as a function of Li_2MnO_3 content, J. Electrochem. Soc. 161 (2014) A318–A325.

[39] L. Chen, S. Chen, D.-Z. Hu, Y.-F. Su, W.-K. Li, Z. Wang, L.-Y. Bao, F. Wu, Crystal structure and electrochemical performance of lithium-rich cathode materials $xLi_2MnO_3{\cdot}(1\text{-}x)LiNi_{0.5}Mn_{0.5}O_2$ (x=0.1-0.8), Acta Phys. - Chim. Sin. 30 (2014) 467–475.

[40] D. Peralta, J.-F. Colin, A. Boulineau, L. Simonin, F. Fabre, J. Bouvet, P. Feydi, M. Chakir, M. Chapuis, S. Patoux, Role of the composition of lithium-rich layered oxide materials on the voltage decay, J. Power Sources 280 (2015) 687–694.

[41] Z.H. Lu, J.R. Dahn, Understanding the anomalous capacity of $Li/Li[Ni_xLi_{(1/3\text{-}2x/3)}Mn_{(2/3\text{-}x/3)}]O_2$ cells using *in situ* X-ray diffraction and electrochemical studies, J. Electrochem. Soc. 149 (2002) A815–A822.

[42] J. Liu, J. Liu, R. Wang, Y. Xia, Degradation and structural evolution of $xLi_2MnO_3{\cdot}(1\text{-}x)LiMn_{1/3}Ni_{1/3}Co_{1/3}O_2$ during cycling, J. Electrochem. Soc. 161 (2014) A160–A167.

[43] J. Liu, L. Chen, M. Hou, F. Wang, R. Che, Y. Xia, General synthesis of $xLi_2MnO_3{\cdot}(1\text{-}x)LiMn_{1/3}Ni_{1/3}Co_{1/3}O_2$ nanomaterials by a molten-salt method: towards a high capacity and high power cathode for rechargeable lithium batteries, J. Mater. Chem. 22 (2012) 25380–25387.

[44] F. Amalraj, D. Kovacheva, M. Talianker, L. Zeiri, J. Grinblat, N. Leifer, G. Goobes, B. Markovsky, D. Aurbach, Synthesis of integrated cathode materials $xLi_2MnO_3{\cdot}(1\text{-}x)LiMn_{1/3}Ni_{1/3}Co_{1/3}O_2$ (x = 0.3, 0.5, 0.7) and studies of their electrochemical behavior, J. Electrochem. Soc. 157 (2010). S19-S19.

[45] L. Riekehr, J. Liu, B. Schwarz, F. Sigel, I. Kerkamm, Y. Xia, H. Ehrenberg, Effect of pristine nanostructure on first cycle electrochemical characteristics of lithium-rich lithium-nickel-cobalt-manganese-oxide cathode ceramics for lithium ion batteries, J. Power Sources 306 (2016) 135–147.

[46] B. Li, Y. Yu, J. Zhao, Facile synthesis of spherical $xLi_2MnO_3{\cdot}(1\text{-}x)Li(Mn_{0.33}Co_{0.33}Ni_{0.33})O_2$ as cathode materials for lithium-ion batteries with improved electrochemical performance, J. Power Sources 275 (2015) 64–72.

[47] M. Lengyel, X. Zhang, G. Atlas, H.L. Bretscher, I. Belharouak, R.L. Axelbaum, Composition optimization of layered lithium nickel manganese cobalt oxide materials synthesized via ultrasonic spray pyrolysis, J. Electrochem. Soc. 161 (2014) A1338–A1349.

[48] Y.S. Meng, G. Ceder, C.P. Grey, W.S. Yoon, M. Jiang, J. Breger, Y. Shao-Horn, Cation ordering in layered O3 $LiNi_xLi_{1/3\text{-}2x/3}Mn_{2/3\text{-}x/3}O_2$ ($0 <= x <= 1/2$) compounds, Chem. Mater. 17 (2005) 2386–2394.

[49] W. Yang, T.P. Devereaux, Anionic and cationic redox and interfaces in batteries: advances from soft X-ray absorption spectroscopy to resonant inelastic scattering, J. Power Sources 389 (2018) 188–197.

[50] X. Liu, Y.J. Wang, B. Barbiellini, H. Hafiz, S. Basak, J. Liu, T. Richardson, G. Shu, F. Chou, T.-C. Weng, D. Nordlund, D. Sokaras, B. Moritz, T.P. Devereaux, R. Qiao, Y.-D. Chuang, A. Bansil, Z. Hussain, W. Yang, Why $LiFePO_4$ is a safe battery electrode: coulomb repulsion induced electron-state reshuffling upon lithiation, Phys. Chem. Chem. Phys. 17 (2015) 26369–26377.

[51] R. Qiao, Y.-D. Chuang, S. Yan, W. Yang, Soft X-ray irradiation effects of Li_2O_2, Li_2CO_3 and Li_2O revealed by absorption spectroscopy, PLoS One 7 (2012).

[52] W.E. Gent, K. Lim, Y. Liang, Q. Li, T. Barnes, S.-J. Ahn, K.H. Stone, M. McIntire, J. Hong, J.H. Song, Y. Li, A. Mehta, S. Ermon, T. Tyliszczak, D. Kilcoyne, D. Vine, J.-H. Park, S.-K. Doo, M.F. Toney, W. Yang, D. Prendergast, W.C. Chueh, Coupling between oxygen redox and cation migration explains unusual electrochemistry in lithium-rich layered oxides, Nat. Commun. 8 (2017).

[53] J. Xu, M. Sun, R. Qiao, S.E. Renfrew, L. Ma, T. Wu, S. Hwang, D. Nordlund, D. Su, K. Amine, J. Lu, B.D. McCloskey, W. Yang, W. Tong, Elucidating anionic oxygen activity in lithium-rich layered oxides, Nat. Commun. 9 (2018).

[54] X. Rong, J. Liu, E. Hu, Y. Liu, Y. Wang, J. Wu, X. Yu, K. Page, Y.-S. Hu, W. Yang, H. Li, X.-Q. Yang, L. Chen, X. Huang, Structure-induced reversible anionic redox activity in Na layered oxide cathode, Joule 2 (2018) 125–140.

[55] D. Carlier, I. Saadoune, M. Menetrier, C. Delmas, Lithium electrochemical deintercalation from O2 $LiCoO_2$-Structure and physical properties, J. Electrochem. Soc. 149 (2002) A1310–A1320.

[56] H. Chen, M.S. Islam, Lithium extraction mechanism in Li-rich Li_2MnO_3 involving oxygen hole formation and dimerization, Chem. Mater. 28 (2016) 6656–6663.

[57] A.R. Armstrong, M. Holzapfel, P. Novak, C.S. Johnson, S.-H. Kang, M.M. Thackeray, P.G. Bruce, Demonstrating oxygen loss and associated structural reorganization in the lithium battery cathode $LiNi_{0.2}Li_{0.2}Mn_{0.6}O_2$, J. Am. Chem. Soc. 128 (2006) 8694–8698.